Defocused imaging of second harmonic generation from a single nanocrystal

N. Sandeau, L. Le Xuan, D. Chauvat, C. Zhou, J.-F. Roch, and S. Brasselet*

Laboratoire de Photonique Quantique et Moléculaire,
École Normale Supérieure de Cachan, 61 av. du Président Wilson,
94235 Cachan, France

Present adress : Institut Fresnel, MOSAIC
Domaine universitaire St Jérôme,
13397 Marseille Cedex 20, France
**sophie.brasselet@fresnel.fr*

Abstract: We demonstrate the direct imaging of the second harmonic generation radiation from a single nonlinear nanocrystal using defocused nonlinear microscopy. This technique allows the retrieval of complete information on the 3D orientation of a nanocrystal as well as possible deviations from its purely crystalline nature, in a simple experimental implementation. The obtained images are modeled by calculation of the radiation diagram from a nonlinear dipole that accounts for the excitation beam, the crystal symmetry and the particle size. Experimental demonstrations are performed on Potassium Titanyl Phosphase (KTP) nanocrystals. The shape and structure of the radiation images show a strong dependence on both crystal orientation and field polarization state, as expected by the specific nonlinear coherent coupling between the induced dipole and the excitation field polarization state.

© 2007 Optical Society of America

OCIS codes: (180.4315) Nonlinear microscopy; (190.1900) Diagnostic applications of nonlinear optics.

References and links

1. M. Flijrsheimer, C. Radiige, H. Salmen, M. Bösch, R. Terbrack, and H. Fuchs, "In-situ imaging of Langmuir monolayers by second-harmonic microscopy," Thin Solid Films **284**, 659-662 (1996).
2. R. Gauderon, P. B. Lukins, and C. J. R. Sheppard, "Three-dimensional second-harmonic generation imaging with femtosecond laser pulses," Opt. Lett. **23**, 1209-1212 (1998).
3. P.J. Campagnola, M. Wei, A. Lewis, and L.M. Loew, "High-Resolution Nonlinear Imaging of Live Cells by Second Harmonic Generation," Biophys. J. **77**, 3341-3349 (1999).
4. L. Moreaux, O. Sandrea, and J. Mertz, "Membrane Imaging by Second Harmonic Generation Microscopy," J. Opt. Soc. Am. B **17**, 1685-1689 (2000).
5. C. Anceau, S. Brasselet, and J. Zyss, "Local orientational distribution of molecular monolayers probed by nonlinear microscopy," Chem. Phys. Lett. **411**, 98-102 (2005).
6. V. Le Floc'h, S. Brasselet, J.-F. Roch, and J. Zyss, "Monitoring of orientation in molecular ensembles by polarization sensitive nonlinear microscopy," J. Phys.Chem. B **107**, 12403-12410 (2003).
7. P. Stoller, B.M. Kim, A.M. Rubenchik, K.M. Reiser, and L.B. Da Silva, "Polarization-dependent optical second harmonic imaging of a rat-tail tendon," J. Biomed. Opt. **7**, 205-214 (2000).
8. K. Komorowska, S. Brasselet, J. Zyss, L. Pourlsen, M. Jazdzyk, H.J. Egelhaaf, J. Gierschner, and M. Hanack, "Nanometric scale investigation of the nonlinear efficiency of perhydrotriphynylene inclusion compounds," Chem. Phys. **318**, 12-20 (2005).
9. R. M. Williams, W. R. Zipfel, and W. W. Webb, "Interpreting Second-Harmonic Generation Images of Collagen I Fibrils," Biophys. J. **88**, 13771386 (2005).

#85722 - $15.00 USD Received 26 Jul 2007; revised 18 Oct 2007; accepted 18 Oct 2007; published 20 Nov 2007

10. J. Zyss, "Molecular Engineering Implications of Rotational Invariance in Quadratic Nonlinear Optics: from Dipolar to Octupolar Molecules and Materials," J.Chem. Phys. **98**, 6583-6593 (1993)
11. E. Yew, and C. Sheppard, "Effects of axial field components on second harmonic generation microscopy," Opt. Expr. **14**, 1167-1174 (2006).
12. G. Revillod, I. Russier-Antoine, E. Benichou, C. Jonin, and P-F. Brevet, "Investigating the interaction of crystal violet probe molecules on sodium dodecyl sulfate micelles with Hyper-Rayleigh scattering," J. Phys. Chem. B **109**, 5383-5389 (2005).
13. S. Brasselet, V. Le Floc'h, F. Treussart, J.-F. Roch, J. Zyss, E. Botzung-Appert, and A. Ibanez, "In situ diagnostics of the crystalline nature of single organic nanocrystals by nonlinear microscopy," Phys. Rev. Lett. **92**, 207401-204405 (2004).
14. F. Treussart, E. Botzung-Appert, N.T. Ha-Duong, A. Ibanez, J.-F. Roch, and R. Pansu, " Second harmonic generation and fluorescence of CMONS dye nanocrystals grown in a sol-gel thin film ," Chem. Phys. Chem. **4**, 757-760 (2003).
15. E. Delahaye, N. Tancrez, T. Yi, I. Ledoux, J. Zyss, S. Brasselet, and R. Clément, "Second harmonic generation from individual hybrid MnPS3-based nanoparticles investigated by nonlinear microscopy" Chem. Phys. Lett. **429**, 533-537 (2006).
16. L. Le Xuan, F. Marquier, D. Chauvat, S. Brasselet, F. Treussart, S. Perruchas, C. Tard, T. Gacoin, and J.-F. Roch, "Balanced homodyne detection in second harmonic generation microscopy," Appl. Phys. Lett. **89**, 121118-1-3 (2006).
17. J. P. Long, B. S. Simpkins, D. J. Rowenhorst, and P. E. Pehrsson, "Far-field Imaging of Optical Second-Harmonic Generation in Single GaN Nanowires," Nanoletters **7**, 831-836 (2007).
18. L. Le Xuan, C. Zhou, A. Slablab, D. Chauvat, C. Tard, S. Perruchas, T. Gacoin, P. Villeval, and J.-F. Roch, "Photostable blinking-free single nanocrystals for second harmonic microscopy," submitted.
19. S. Brasselet, and J. Zyss, "Nonlinear polarimetry of molecular crystals down to the nanoscale," C. R. Physique **8**, 165-179 (2007). ,
20. M. Böhmer, and J. Enderlein, "Orientation imaging of single molecules by wide-field epifluorescence microscopy," J. Opt. Soc. Am. B **20**, 554-559 (2003).
21. J. Enderlein, and M. Böhmer, "Influence of interface dipole interactions on the efficiency of fluorescence light collection near surfaces," Opt. Lett. **28**, 941-944 (2003).
22. M.A. Lieb, J.M. Zavislan, and L. Novotny, "Single-molecule orientations determined by direct emission pattern imaging," J. Opt. Soc. Am. B **21**, 1210-1215 (2004).
23. X. Brokmann, M.-V. Ehrensperger, J.-P. Hermier, A. Triller, and M. Dahan, "Orientational imaging and tracking of single CdSe nanocrystals by defocused microscopy," Chem. Phys. Lett. **406**, 210214 (2005).
24. J. Enderlein, "Theoretical study of detection of a dipole emitter through an objective with high numerical aperture," Opt. Lett. **25**, 634-637 (2000).
25. H. Vanherzeele, and J. D. Bierlein, "Magnitude of the nonlinear-optical coefficients of $KTiOPO_4$," Opt. Lett. **17**, 982-985 (1992).
26. B. Richards, and E. Wolf, "Electromagnetic diffraction in optical systems. II. Structure of the image field in an aplanetic system," Proc. of the Royal Society of London. Series A. **153**, 358-579 (1959).
27. D.Gachet, N. Sandeau, and H. Rigneault, "Far-field radiation pattern in Coherent Anti-stokes Raman Scattering (CARS) Microscopy," Biomedical Vibrational Spectroscopy III: Advances in Research and Industry, SPIE **6093** 62, (2006).

1. Introduction

Second harmonic generation (SHG) microscopy is now recognized as an appropriate technique for the investigation of molecular, biomolecular and inorganic media at the sub-micrometric scale [1, 2, 3, 4, 5, 6]. This technique, based on two-photon excitation in a microscope using high numerical aperture optics, benefits from an intrinsic resolution of a few hundreds of nanometers due to the nonlinear nature of the excitation. An additional factor of contrast is provided by SHG comparing to two-photon fluorescence since in the dipolar approximation it cancels out in centrosymmetric media. One of the main interest of SHG microscopy is therefore the possibility to reveal locally molecular alignment and structural information with a high angular accuracy [7, 6, 8, 5, 9]. This specificity of the SHG signal originates from the nonlinear susceptibility $\chi^{(2)}$ of the material, a second-order tensor which coefficients are related to the medium symmetry and structure. In particular, a purely one-dimensional system of $C_{\infty v}$ symmetry exhibits a single $\chi^{(2)}$ tensor coefficient, whereas a material of more complex multipolar symmetry contains multiple tensorial $\chi^{(2)}_{IJK}$ terms (with I,J,K denoting spatial directions in the

#85722 - $15.00 USD Received 26 Jul 2007; revised 18 Oct 2007; accepted 18 Oct 2007; published 20 Nov 2007
(C) 2007 OSA

3D space) [10]. Such coefficients consequently couple to multiple polarization directions of the incident field $\vec{E}^{\omega}$. This has been recently illustrated in a vectorial treatment of SHG which emphasizes that under a high numerical aperture illumination (typically N.A. = 1.4), a nonlinear tensorial coupling with the axial component of the optical field leads to non-negligible axial components of the nonlinear induced dipole [11].

Measurements of nonlinear properties of nano-objects and molecules have mostly relied on Hyper Rayleigh Scattering, which is a sensitive technique that however suffers from the fact that information is retrieved from an average over an ensemble of nano-objects [12]. Recently, the possibility of using SHG microscopy to avoid this averaging and access to information from individual nano-objects has been demonstrated on nanocrystals of sizes down to tens of nanometers in organics as well as hybrid materials [13, 14, 15], and more recently on inorganic nano-scale crystals [16, 17]. Nonlinear nanocrystals have various potential interests as bright and photostable nano-sources, in particular due to the high contrast that they can provide with respect to a centro-symmetric background, as well as the potential absence of photobleaching in non-resonant excitation conditions [16, 18]. The proper use of such nano-sources however necessitates a knowledge of their crystalline quality and three dimensional orientation.

We have previously demonstrated that in-plane polarimetric measurements of the second harmonic generation signal from a single organic nanocrystal can provide information on its orientation [13]. This measurement is based on the analysis of the projection of the nonlinear dipole in the sample plane, and therefore cannot lead to the full 3D information in the case of symmetries close to one-dimensional structures. In addition, the use of two-photon fluorescence polarization properties of the studied systems in conjunction with SHG provides a complementary diagnostic of mono-crystallinity in such individual nano-objects [13, 19]. Such scheme however necessitates to work under resonant conditions.

In the present work, we show that a defocused imaging of the SHG emission from an individual nanocrystal is capable of identifying the 3D orientation *for any crystalline symmetry*, and provides a diagnostics for crystallinity even *without the need of associated two-photon fluorescence signals*. This technique is based on the imaging of the nonlinear induced dipole radiation on a defocused CCD camera, adapted from a method already developed for 3D orientation imaging of fluorescent single molecules and nanocrystals [20, 21, 22, 23]. The specificity of applying this technique to SHG is that the imaged pattern is expected to depend strongly on the incident fundamental polarization state, due to the coherent coupling between the $\chi^{(2)}$ nonlinear tensor and the incoming field polarization components. This imaging technique is thus a tool for 3D orientation determination and efficient structural investigation.

Demonstration of the technique is realized on Potassium-Titanyl-Phosphase (KTP) nanocrystals of 80 nm size dispersed in a polymer matrix [16]. The shape of SHG radiation patterns are analyzed for individual nanocrystals, for a controlled incident fundamental polarization. We describe how structural and orientational information can be retrieved from the experimental data using a model based on a propagation calculation of the induced nonlinear field through the microscope optics.

2. Principle of nonlinear defocused imaging

The defocused imaging technique is based on an inverted microscopy configuration where a high numerical aperture infinity-corrected objective is used to provide two-photon excitation of an individual crystal placed at the center of its focus spot (Fig. 1(a)). This objective also collects the induced SHG radiation in the backward direction. The tube lens of the microscope is used as an imaging lens. The principle of defocused imaging is to record an image of the SHG radiation in a plane located away from the focus image point of the imaging lens, as depicted in Fig. 1(a). The pattern formed on the defocused image plane of the microscope originates from

#85722 - $15.00 USD Received 26 Jul 2007; revised 18 Oct 2007; accepted 18 Oct 2007; published 20 Nov 2007
(C) 2007 OSA

the coherent addition of the electric fields radiated by each individual microscopic nonlinear induced dipole in the crystal. The calculation of the radiated field from a single nonlinear dipole $\vec{p}^{2\omega}(\vec{r})$ located in the objective object plane at a distance $\vec{r}$ from the optical axis, and the consequent spatial distribution of the emitted field on the defocused image plane after passing through the objective O and imaging lens L, are based on a vectorial model [21, 24] detailed in the appendix.

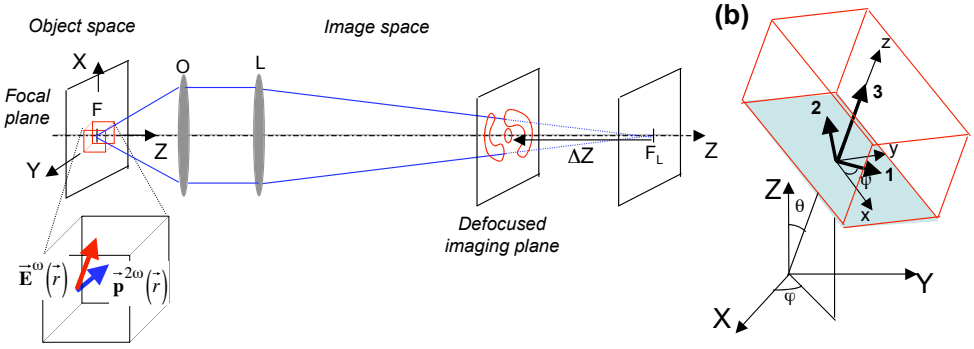

Fig. 1. (a) Simplified scheme of the defocused imaging microscope. O : high numerical aperture microscope objective, L : imaging lens. (b) Orientation Euler angles (θ,ϕ,ψ) of the KTP crystalline unit cell $(1,2,3)$ in the macroscopic frame (X,Y,Z).

The orientation of the nonlinear induced dipole $\vec{p}^{\,2\omega}(\vec{r})$ depends on the crystal symmetry, its orientation, as well as on the exciting field polarization, as can be seen in the tensorial product expression of the macroscopic I component :

$$p_I^{2\omega}(\vec{r}) = \sum_{J,K} \chi^{(2)}_{IJK}(\theta,\varphi,\psi) E_J^{\omega}(\vec{r})\, E_K^{\omega}(\vec{r}) \tag{1}$$

where $(I,J,K) = (X,Y,Z)$. (θ,φ,ψ) is the Euler set of angles defining the orientation of the crystalline unit-cell in the macroscopic frame (X,Y,Z) (Fig. 1(b)), and $E^{\omega}_{J,K}(\vec{r})$ are the incident macroscopic field polarization components at the location $\vec{r}$ in the crystal. In this expression, local field factors are not explicited and are considered to be scalar quantities, which is a first approximation in a birefringent medium.

The macroscopic $\chi^{(2)}_{IJK}(\theta,\varphi,\psi)$ contributions appearing in equation (1) can be related to the microscopic known $\chi^{(2)}_{ijk}$ coefficients (with $(i,j,k) = (1,2,3)$ being the unit-cell axes as depicted in Fig. 1(b)) by the tensorial rotation relation [10]:

$$\chi^{(2)}_{IJK}(\theta,\varphi,\psi) = \sum_{i,j,k} \chi^{(2)}_{ijk} (\vec{i}\cdot\vec{I})(\vec{j}\cdot\vec{J})(\vec{k}\cdot\vec{K})(\theta,\varphi,\psi) \tag{2}$$

In the present work we use the $\chi^{(2)}_{ijk}$ coefficients from the KTP material given in reference [25]. In this crystal of orthorhombic nature, the main nonlinear tensorial coefficient is $\chi^{(2)}_{333}$ involving only the "3" axis, whereas the perpendicular contributions involving the "(1,2)" axes are at least 4 times weaker in magnitude. This symmetry therefore implies a preferable SHG response at the microscopic scale along to the "3" axis, however with possible coupling along the other axes.

In equation (1), the spatial dependence of the incoming field at the fundamental frequency ω in the object plane is calculated using the approach developed by Richards and Wolf [26],

#85722 - $15.00 USD Received 26 Jul 2007; revised 18 Oct 2007; accepted 18 Oct 2007; published 20 Nov 2007
(C) 2007 OSA

accounting for a Gaussian beam shape in the superposition of plane waves [27]. Its polarization spatial distribution, which is known to be inhomogeneous away from the optical axis [26], is also accounted for since it can potentially affect the SHG emission pattern from a crystal of size approaching the diffraction limit of the objective. Calculated defocused images for a KTP nanocrystal of growing size tilted by an angle (θ = 45°,φ = 0°,ψ = 0°) are represented in Fig. 2(a-c). The nanocrystal is modeled by a cubic shape sampled by placing one individual dipole every nm^3 within this cube. The crystal is supposed to be embedded in an infinite medium of matching index, thus assuming that no interface lies closely to the crystal, which would affect its radiation features. This is ensured in practice by using a thick polymer film as an embedding environment. These images are calculated for a defocused negative distance of $\Delta Z = -15$ mm towards the objective in the Z direction, as performed in the experiments. Positive defocusing would provide identical information.

The patterns of the defocused images from nanocrystals of different sizes have similar features, with a symmetry axis along the direction of the nonlinear induced dipole. The ring-structured shape is representative of the 45° tilt angle of the "3" axis of the crystal with respect to Z. This rough similarity among the observed pattern with respect to crystal size shows that radiation imaging can be used as a robust technique to determine orientation independently on the crystal size, provided that it lies below 150-200 nm. Above this size range, the fine structure of the observed rings is seen to clearly deviate from the single dipole model. In the following experimental study dedicated to KTP nanocrystals of about 80 nm sizes, the system can therefore be described for qualitative analysis by the emission of a single dipole placed at the center F of the focal spot of the objective. Accounting for the crystal size is only needed in order to further analyze the fine structure of the patterns. Note that for sizes above the 150-200 nm range, the epi-detection used in the present work is no longer adequate (Fig. 2(d-f)), as the coherent build-up of the signal as well as phase matching properties favor a forward-emission scheme. In the present case of 80 nm nanocrystals, the portion of angular radiation in the backward direction is however still significative, which allows the epi-detection scheme.

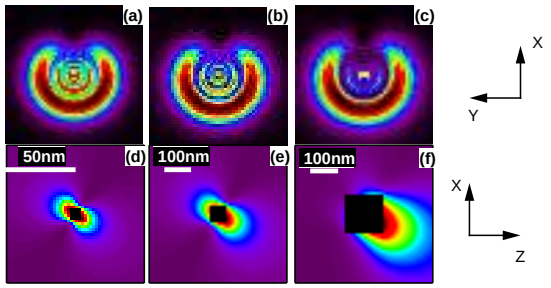

Fig. 2. (a-c) : calculated emission patterns from a single KTP nanocrystal centered on F, with orientation (θ =45°,φ = 0°,ψ = 0°), for increasing sizes : (a) 10 nm (b) 80 nm, (c) 150 nm. The KTP nanocrystal is excited by a polarization in the X direction. The images size is 600×600 μm^2. (d-f) : Angular dependence of the SHG emission in the (X,Z) plane for the same nanocrystals. The black squares represent the shape of the nanocrystals, chosen arbitrarily as cubic for the simulation. The color scale is normalized to the maximum value of the intensity for each image. The parameters used in the vectorial model calculation are the experimental ones : objective magnification $m = 100$, numerical aperture $N.A. = 1.4$, imaging lens focal length $f_L = 180$ nm, defocusing distance in the image space $\Delta Z = -15$ mm, incident fundamental wavelength λ =945 nm, embedding polymer index n =1.5.

#85722 - $15.00 USD Received 26 Jul 2007; revised 18 Oct 2007; accepted 18 Oct 2007; published 20 Nov 2007
(C) 2007 OSA

3. Experimental results

The experimental setup is an inverted two-photon excitation microscope coupled to two possible exit ports, one for in-plane polarimetric analysis [13] and one for defocused imaging. A mode-locked Ti:Sa laser beam of about 100 fs pulses at a fundamental wavelength of 945 nm with a 80 MHz repetition rate is focused on the sample by a high numerical aperture oil immersion objective (*N.A.* 1.4), leading to a spatial resolution of approximatively 300 nm. The typical average incident power is about 1mW. The SHG signal from the sample is collected by the same objective and filtered around the 2ω harmonic wavelength by band pass and interference filters.

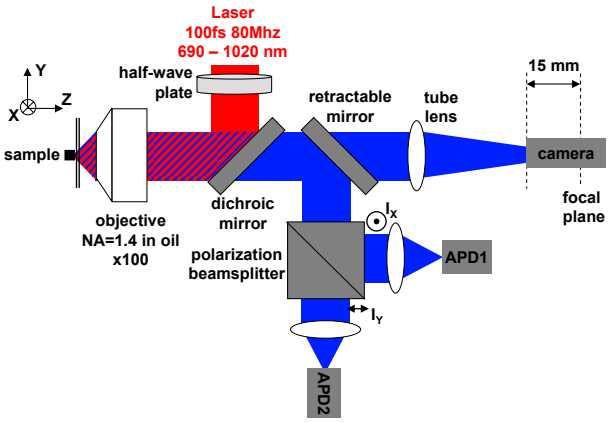

Fig. 3. Schematic representation of the polarimetric and defocused imaging measurements. *Z* is the optical axis, perpendicular to the sample. The *X* and *Y* axes, lying in the sample plane, provide the analysis framework for the polarization directions detected by the two avalanche photodiodes *APD*1 and *APD*2, working in the single photon counting mode.

The KTP nanocrystals are extracted from a raw powder of KTP resulting from a flux growth process. A size selection process results in a colloidal solution containing KTP nanocrystals of size (80±15) nm mixed with a polyvinylpyrolidone polymer (PVP) in isopropanol [18]. Evaporation of a drop of this solution on a glass cover slip leads to KTP nanocrystals well embedded in a thick polymer film. The PVP environment ensures that no interface effect affects their emission pattern. The concentration of nanocrystals is chosen such as they are isolated from each other, and thus localized by diffraction-limited bright SHG spots. After identification of an isolated nanocrystal, the scanning stage is used to place it at the center of the focused incident beam, where polarimetry and defocused imaging are independently performed.

For in-plane polarimetric analysis, the SHG signal is directed to a polarizing beamsplitter separating the collected signal into two polarization states *X* and *Y* on two avalanche photodiodes. The corresponding signals I_X and I_Y are recorded while the incident polarization is rotated in its plane from 0° (along *X*) to 360°.

For defocused imaging, the SHG signal is directed towards a sensitive CCD camera (512×512 pixels, $13\times13\mu\mathrm{m}^2$ pixel size, thermoelectrically cooled) which is translated by 15 mm towards the objective, so as to obtain a contrasted image of about $600\times600\mu\mathrm{m}^2$ size.

Figure 4 exhibits measured defocused images from a single KTP nanocrystal for different polarization orientations of the incoming fundamental field in the sample plane. Different features appear on these images. First, they exhibit a symmetry axis which orientation in the sample plane is related to the nanocrystal in-plane orientation. Second, the structure of the image, in particular its rings feature, is characteristic of a nanocrystal exhibiting out-of-plane orientation with $\theta\neq0°$. Third, the symmetry axis of the structure rotates when changing the incident po-

#85722 - $15.00 USD Received 26 Jul 2007; revised 18 Oct 2007; accepted 18 Oct 2007; published 20 Nov 2007
(C) 2007 OSA

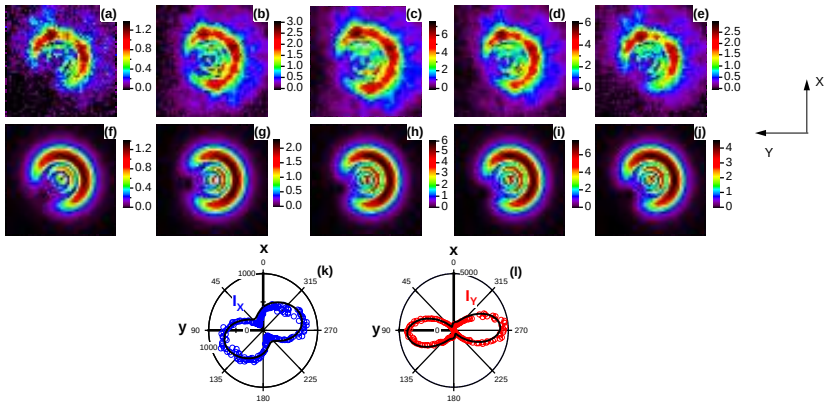

Fig. 4. (a-e) Experimental defocused images of a KTP nanocrystal for several incident polarization directions relative to the X axis: (a) 0°, (b) 60°, (c) 90°, (d) 120° and (e) 150°. The images sizes are $600\times600\mu m^2$. The integration time for each image is 5 s. (f-j) Corresponding calculated images, leading to the orientation parameters ($\theta = 30^\circ \pm 5^\circ, \phi = 115^\circ \pm 5^\circ, \psi = 90^\circ \pm 20^\circ$). (k,l) Experimental polarimetric analysis I_X and I_Y of this nanocrystal (circle markers) and corresponding calculated polarization responses (lines) for the Euler set of angles deduced from the defocused imaging analysis.

larization direction. This is characteristic from a nonlinear coherently induced dipole emission as opposed to a single fluorescent dipole, since the KTP multipolar symmetry structure allows coherent nonlinear coupling with various incident field polarization directions.

Starting from the ring pattern observation for a first estimate of the 3D orientation parameter, the emission pattern calculation (Fig. 4(f-j)) is then implemented to manually adjust at best the measured images (Fig. 4(a-e)). This leads to a 3D orientation determination with error margins of $\pm5^\circ$ at maximum for θ and ϕ. This error is much larger for the ψ Euler angle (from $\pm10^\circ$ to $\pm50^\circ$), which is specific to the case of KTP for which there is only a weak difference between nonlinear coefficients involving the "(1,2)" directions perpendicular to the main "3" axis [25]. The ψ angle is thus not strongly relevant by nature in the present study. In order to confirm the values for the obtained orientation angles, they were used as input parameters to calculate the in-plane polarimetric SHG response of the measured nanocrystal. The corresponding angular dependencies agree well with the experimental data (Fig. 4(k,l)). Note that a direct determination of the Euler angles from such polarimetric responses would have been more delicate since the KTP symmetry exhibits several ambiguous situations when projected in the sample plane. This points-out the advantages of the defocused imaging technique, which encompasses a complete 3D coupling information in the observed pattern shapes.

The application of this technique to orientation measurements of more than ten isolated nanocrystals shows furthermore that only up to two incident polarization angles are necessary for an unambiguous angular determination. This is illustrated in Fig. 5 for two different nanocrystals, where the corresponding calculated image could be found with a good agreement with the experimental data.

At last in addition to 3D orientation determination, such a technique presents the unique property of providing a diagnostics for the crystalline quality of an isolated nano-object. Indeed the presence of nanocrystals of different orientations in a same focus point would strongly affect the defocused image properties described above, and allow a direct conclusion on the mono-crystallinity of the observed object. This is illustrated in Fig. 6, representative of a nano-

#85722 - $15.00 USD Received 26 Jul 2007; revised 18 Oct 2007; accepted 18 Oct 2007; published 20 Nov 2007
(C) 2007 OSA

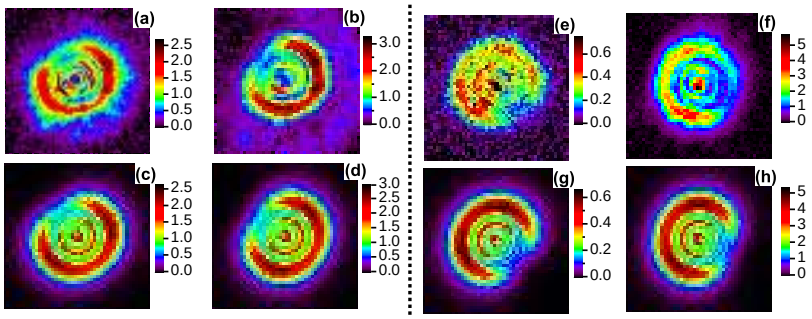

Fig. 5. (a-d) and (e-h) examples of defocused images of two single KTP nanocrystals. Experimental (top) and calculated (bottom) images are obtained for different incident polarization directions relative to the X axis: (a,c,e,g) 0° and (b,d,f,h) 90°. The nanocrystals are found to be oriented along the ($\theta = 67° \pm 5°, \phi = 46° \pm 5°, \psi = 45° \pm 20°$) angles (left) and ($\theta = -55° \pm 5°, \phi = 65° \pm 5°, \psi = 90° \pm 20°$) angles (right). The size of the images is $600 \times 600 \mu m^2$.

metric size KTP for which images are deprived from a symmetry axis and deviate from the previously observed ring structures. Such images are representative of the presence of at least two KTP nanocrystals in the focus point of the objective, which could not be revealed by the sole observation of the diffraction-limited spot size.

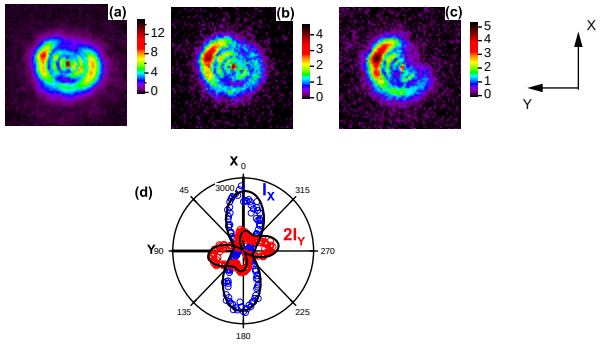

Fig. 6. (a-c) Defocused images of a nanocrystal for several incident polarization directions relative to the X (horizontal) axis: (a) 0°, (b) 306° and (c) 90°. The images sizes are $800 \times 800 \mu m^2$. This nano-object is visibly constituted of several distinct sub-domains. (d) Polarimetric analysis of this nano-cluster of nanocrystals. The adjustment of polarimetric responses (black line) is done using two nanocrystals 1 and 2 of respective orientations ($\theta_1 = 20°, \phi_1 = 260°, \psi_1 = 0°$) and ($\theta_2 = 45°, \phi_2 = 350°, \psi_2 = 0°$).

A finer observation can furthermore conclude that in this two-KTP nanocrystals picture, one of them is likely to lie close to the vertical X axis of the images, since the SHG pattern approaches a ring structure for a X-polarized excitation. The other KTP nanoparticle is preferentially excited for a polarization angle close to 45° (relative to X), and therefore manifests with larger signals in Fig. 6(b,c) as the excitation angle increases. This deviation from a monocrystalline structure is confirmed in the polarimetric response of such a nano-object, which curve cannot be fitted using a single KTP unit-cell model, but rather by two or more nanocrystals orientations. The polarimetric responses could indeed be adjusted by the coherent addition

#85722 - $15.00 USD Received 26 Jul 2007; revised 18 Oct 2007; accepted 18 Oct 2007; published 20 Nov 2007
(C) 2007 OSA

of two nanocrystals of respective orientations given in the caption of Fig. 6, which lie close to the ones estimated using the defocused images. Note that while the polarimetric adjustments reveal only one possible solution for the respective orientations for the two nanocrystals, the defocused images provide directly a finer information.

4. Conclusion

We have demonstrated that defocused imaging of second harmonic generation radiation from a single KTP nanocrystal can provide a direct retrieval of its 3D orientation. This orientation information, based on the knowledge of the nano-object crystalline symmetry, can thus be used as a complete characterization of the polarization state from a nonlinear nanosource. In addition, we show that this technique provides the unique possibility to inform on the mono-crystallinity nature of a nano-object. Finally, this analysis method is a promising tool of analysis of the vectorial electric-field nature from an unknown electromagnetic incident radiation, taking advantage of the rich features appearing from the nonlinear coupling between matter at the subwavelength scale and complex polarization components.

Acknowledgements

We are grateful to Philippe Villeval (Cristal Laser, Nancy, France) for providing us with the KTP powder and to Thierry Gacoin, Sandrine Perruchas and Cédric Tard (LPMC, Ecole Polytechnique, France) for the fabrication of the nanocrystal colloidal solution. We thank Yannick Dumeige for his contribution on defocused radiation numerical calculations.

Appendix

A nonlinear induced dipole denoted $\vec{p}^{2\omega}$ is located at a position ($\vec{r}$) from the center F of the object plane, which is at the focal point of the microscope objective O. This nonlinear dipole is supposed to be generated from an excitation using the same objective in an inverted microscope geometry.

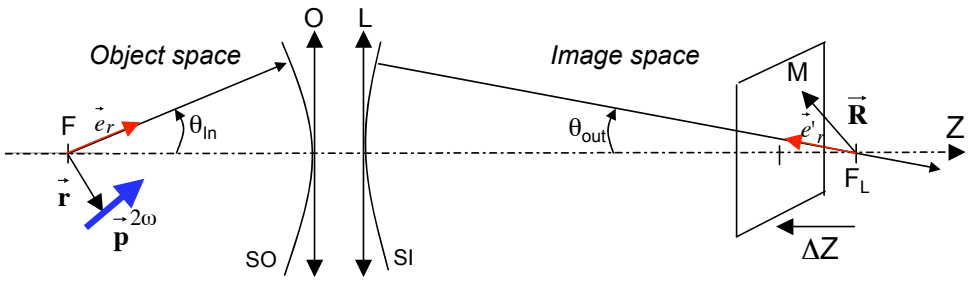

Fig. 7. Optical scheme of the defocused imaging microscope. O : high numerical aperture microscope objective, L : imaging lens. For seek of simplicity in the dipole radiation calculation, the distance between O and L is assumed to be equal to zero. The reference spheres of O and L, named respectively SO and SI, are respectively centered on F and F_L.

After the SHG emission is collected by the objective, the tube lens L images this radiation on the image plane centered on the focus point F_L (Fig. 7). The defocused image is then formed in a plane translated in the Z propagating direction by a distance ΔZ from this position.

Neglecting non-propagative waves, the radiated electric field in the object space $\vec{E}_{in}^{2\omega}$ expressed on the reference sphere SO of the objective, is given by [21, 24]:

#85722 - $15.00 USD Received 26 Jul 2007; revised 18 Oct 2007; accepted 18 Oct 2007; published 20 Nov 2007
(C) 2007 OSA

$$\vec{E}_{in}^{2\omega}(\vec{r}) \propto k^2 \frac{exp\left[ik\left|f\vec{e}_r - \vec{r}\right|\right]}{\left|f\vec{e}_r - \vec{r}\right|^3} \left(f\vec{e}_r - \vec{r}\right) \times \left[\left(f\vec{e}_r - \vec{r}\right) \times \vec{p}^{2\omega}(\vec{r})\right] \tag{3}$$

with $k = 2\omega/c$ the nonlinear wave vector modulus in the vacuum, f the focal length of the objective and $\vec{e}_r$ the radial vector of the spherical base associated to the sphere *SO*. To model the propagation in the image space, the electric field is then calculated on the reference sphere *SI* centered on the focus F_L of the imaging lens. This field denoted $\vec{E}_{out}^{2\omega}$ is:

$$\vec{E}_{out}^{2\omega}(\vec{r}) = m\sqrt{\frac{\cos\theta_{out}}{n\cos\theta_{in}}} \left[\left(\vec{E}_{in}^{2\omega}(\vec{r}) \cdot \vec{e}_r\right)\vec{e}'_r + \left(\vec{E}_{in}^{2\omega}(\vec{r}) \cdot \vec{e}_\theta\right)\vec{e}'_\theta + \left(\vec{E}_{in}^{2\omega}(\vec{r}) \cdot \vec{e}_\varphi\right)\vec{e}_\varphi\right], \tag{4}$$

where θ_{in} and θ_{out} define the object and image angles, m is the microscope magnification and n the refractive index in the object space. $(\vec{e}_r, \vec{e}_\theta, \vec{e}_\varphi)$ and $(\vec{e}'_r, \vec{e}'_\theta, \vec{e}_\varphi)$ are the spherical bases respectively associated with corresponding points on the spheres *SO* and *SI*. In equation (6), the square root is introduced to be in accordance with the geometrical optics intensity law [26]. Finally the electric field in each point M of the defocused image plane defined by the vector $\vec{R} = \overrightarrow{F_L M}$, is given by :

$$\vec{E}^{2\omega}(\vec{R}, \vec{r}) \propto \iint_{\Omega_{out}} \vec{E}_{in}^{2\omega}(\vec{r}) \exp\left[i(\vec{k}' \cdot \vec{R})\right] dk'_X dk'_Z, \tag{5}$$

where Ω_{out} is the image solid angle delimited by the imaging lens aperture of focal distance f_L, and $\vec{k}'$ is the wave vector in the image space defined by:

$$\vec{k}' = k \frac{f_L \vec{e}'_r - \vec{R}}{\sqrt{f_L^2 - 2 f_L \left(\vec{e}'_r \cdot \vec{R}\right) + R^2}} \tag{6}$$

Note that in this model, the f_L focal distance is large enough comparing to ΔZ and R such as a planar wave summation is allowed.

#85722 - $15.00 USD Received 26 Jul 2007; revised 18 Oct 2007; accepted 18 Oct 2007; published 20 Nov 2007
(C) 2007 OSA